

CFD Simulation of Subcooled Boiling Flow in Nuclear Fuel Bundle

W. K. In*, C. H. Shin* and C. Y. Lee*
Corresponding author: wkin@kaeri.re.kr

* Korea Atomic Energy Research Institute, Rep. of Korea.

Abstract: A Computational Fluid Dynamics (CFD) analysis was performed to simulate the subcooled boiling flow in fuel bundles for a Pressurized Water Reactor (PWR) and Boiling Water Reactor (BWR). The CFD simulation predicted the steady-state void distribution in the subchannels of the PWR and BWR fuel bundles. The CFD prediction shows a higher void fraction near the heated wall and a migration of the void in the subchannel gap region. The CFD prediction of the void fraction for the PWR subchannel agrees with the measured values within 10% for low inlet subcooling. The CFD simulation for the BWR fuel bundle reproduced the overall radial void distribution trend which shows less vapor in the central part of the bundle and more vapor in the periphery. However, a comparison of the detailed subchannel void distribution shows a somewhat large discrepancy between the CFD and the experimental results.

Keywords: Subcooled Boiling, Computational Fluid Dynamics, Fuel Bundle, Void Fraction, Subchannel.

1 Introduction

A subcooled boiling flow in a rod bundle is an important phenomenon in a nuclear reactor system for the safe and reliable operation. Most nuclear fuel elements loaded in the reactor generally consist of rod bundles with the coolant flowing axially through the subchannels formed between the rods. The fuel rods are arranged in either square or equilateral triangular pitched arrays. Subcooled boiling may be encountered in nuclear reactors under certain conditions. An understanding of the three-dimensional distributions of the flow and phases in the rod bundles, used especially as nuclear fuel elements, is of major interest to the nuclear power industry for their safe and reliable operation. Recently, there have been some studies using CFD in the multi-dimensional analysis of multiphase flow problems. The application of CFD to multiphase flows still requires extensive validation of the computational technique and the closure models as outlined by Yadigaroglu *et al.* [1].

There have been some numerical studies on high-pressure and low-pressure subcooled boiling flows in a simple geometry. Kurul [2] formulated a multidimensional two-fluid model and applied this model to various subcooled boiling phenomena in a heated channel. He also proposed heat transfer modes at a wall and presented a mechanistic model for a wall heat transfer during a forced-convection flow. Anglart [3] applied a multidimensional two-fluid model to a high-pressure (4.5 MPa) boiling bubbly flow in vertical tubes and showed a good agreement between the predictions and measurements of the temperature and void distribution. Anglart and Nylund [4] implemented a two-fluid model into a commercial CFD code and predicted the void distribution in a circular channel with a single heated rod and circular channels with six heated rods with a system pressure of approximately 5 MPa. They predicted void fraction distributions in the subcooled and bulk boiling regions that show a satisfactory agreement with the measurements. Yeoh and Tu [5] employed a three-dimensional two-

fluid model coupled with population balance equations to predict a subcooled boiling flow at a low pressure in a vertical annular channel with the influence of bubble coalescence and break-up. Using the boiling model implemented in the CFD code, CFX-4, Krepper *et al.* [6] simulated boiling experiments in a heated tube and channel around a heated rod. Comparisons with the experiments showed good agreement for pressures at about 1.5 to 5 Mpa, but a significant underestimation of the volume fraction for lower pressures. He also pointed out that the largest influences are found for the bubble departure diameter and mean bubble diameter.

OECD/NEA and US NRC organized international benchmark programs [7, 8] for PWR Subchannel and Bundle Tests (PSBT) and BWR Full-size Fine-mesh Bundle Tests (BFBT). The void distribution benchmark provides measured void fraction data over a wide range of operating conditions in a single subchannel and fuel bundle. This CFD study simulates the boiling flows in four different types of single subchannel for the PSBT benchmark and in the BWR 8x8 fuel-rod bundle. The CFD predictions of the void distribution are compared with the PSBT and BFBT measurements. A CFD code, ANSYS CFX [9] was used to predict the void distribution inside the single subchannel of the PSBT and 8x8 rod bundle of the BFBT.

2 Computational Multiphase Flow Model

The multiphase flow model used in this CFD analysis is a two-fluid model in which liquid (water) and vapour (steam) are considered as continuous and dispersed fluids, respectively. The two-fluid model uses the interfacial area per unit volume between the phases to model the interfacial transfer of momentum, heat and mass. The interfacial momentum transfer rates included in this CFD simulation are drag force, lift force, wall lubrication force and turbulent dispersion force. Heat transfer across a phase boundary is predicted using an inter-phase heat transfer coefficient and an interfacial area. The inter-phase mass transfer is calculated depending on the liquid temperature, i.e., bulk condensation or evaporation. A wall boiling model is also employed to simulate the bubble generation on a heated wall surface. The wall heat is assumed to be partitioned into three parts, i.e., convective, quenching and evaporative heat transfers.

2.1 Two-Fluid Model and Closure Models

The hydrodynamic conservation equations of mass, momentum and energy for each phase can be written as

$$\frac{\partial}{\partial t}(\alpha_k \rho_k) + \nabla \cdot (\alpha_k \rho_k U_k) = \sum_{j=1, j \neq k}^{N_p} (\Gamma_{kj} - \Gamma_{jk}) \quad (1)$$

$$\begin{aligned} \frac{\partial}{\partial t}(\alpha_k \rho_k U_k) + \nabla \cdot (\alpha_k \rho_k U_k U_k) = & \nabla \cdot [\alpha_k \mu_k^e (\nabla U_k + (\nabla U_k)^T)] - \alpha_k \nabla p_k + \alpha_k \rho_k g \\ & + \sum_{j=1, j \neq k}^{N_p} (\Gamma_{kj} U_j - \Gamma_{jk} U_k) + \sum_{j=1, j \neq k}^{N_p} M_{kj} \end{aligned} \quad (2)$$

$$\frac{\partial}{\partial t}(\alpha_k \rho_k H_k) + \nabla \cdot (\alpha_k \rho_k U_k H_k - \alpha_k \lambda_k^e \nabla T_k) = \frac{\partial}{\partial t}(\alpha_k p_k) + E_k + \sum_{j=1, j \neq k}^{N_p} (\Gamma_{kj} H_j - \Gamma_{jk} H_k) + \sum_{j=1, j \neq k}^{N_p} Q_{kj} \quad (3)$$

Here, α_k, p_k, U_k, T_k , and H_k are the volume fraction, pressure, velocity, temperature, and enthalpy of phase k , respectively, and N_p is the number of phases. Γ_{kj} , M_{kj} , and Q_{kj} are the inter-phase transfer of the mass, momentum, and energy from phase j to phase k , and μ_k^e and λ_k^e are the effective viscosity and thermal conductivity of phase k , respectively. Additional variables are the gravitational acceleration, g , and the heat source to phase k , E_k .

The multiphase flow model based on the conservation equations (1)-(3) requires constitutive equations to achieve closure. The accuracy of the multiphase flow model largely depends on how to model the constitutive terms including the phase interaction terms (Γ_{kj} , M_{kj} and Q_{kj}). Since the present CFD analysis is to simulate the vapor-liquid two-phase flow in a rod-bundle geometry, the closure relationships for the interaction terms between a continuous liquid phase and a dispersed vapor phase are required. The closure models are derived for the transport of the momentum, energy, and mass of each phase across the interfaces. A closure model for two-phase turbulence is also required.

The interphase momentum transfer in eq. (2) indicates the rate of the momentum transfer per unit volume at the interface, which is expressed as a superposition of the terms representing different physical mechanisms. The individual interfacial forces are the drag force, virtual mass force, lift force, lubrication force, and turbulent dispersion force, respectively.

$$M_{lg}^d = M_{lg}^d + M_{lg}^{vm} + M_{lg}^L + M_{lg}^{LW} + M_{lg}^{TD} \quad (4)$$

The total drag force per unit volume on the liquid or vapour can be expressed as (Ishii and Mishima [10])

$$M_{lg}^d = -M_{gl}^d = \frac{3}{4} \frac{C_D}{d_b} \alpha_g \rho_l |U_g - U_l| (U_g - U_l) \quad (5)$$

Here, C_D and d_b are the drag force coefficient and mean vapour bubble diameter, respectively. The drag coefficient is obtained from the correlation for the viscous flow region and its modification for a high spherical particle (bubble) concentration (Ishii and Zuber [11]), i.e.,

$$C_D = \frac{24}{\text{Re}_m} (1 + 0.15 \text{Re}_m^{0.687}) \quad (6)$$

$$\text{Re}_m = \frac{\rho_l |U_g - U_l| d_b}{\mu_m} \quad (7)$$

Here, μ_m is a mixture viscosity. The virtual mass force is neglected in this study because the virtual mass force is insignificant for the lateral phase distribution.

The lift force can be written as (Zun [12]),

$$M_{lg}^L = -M_{gl}^L = C_L \alpha_g \rho_l (U_g - U_l) \times (\nabla \times U_l) \quad (8)$$

Here, C_L is the lift force coefficient, which was set to 0.06 [6]. This force from the ‘‘shear’’ lift is perpendicular to the rotation vector and the bubble’s velocity vector. Recently, Tomiyama *et al.* [13] and Hibiki and Ishii [14] evaluated the net lift coefficient, i.e., the sum of shear- and wake-induced lift coefficient, and proposed a correlation yielding the bubble diameter dependency. They showed that the net lift coefficient changes its sign from positive to negative for large bubbles.

The term M_{lg}^{LW} represents the wall lubrication force that is in the normal direction away from a wall and decays with the distance from the wall. This force accounts for the change of the lift force near a wall owing to the change of velocity distribution around the vapour bubble. The force is given by (Antal *et al.*, [15])

$$M_{lg}^{LW} = -M_{gl}^{LW} = \frac{\alpha_g \rho_l (U_g - U_l)^2}{d_b} \cdot \text{Max} \left(C_{w1} + C_{w2} \frac{d_b}{y_w}, 0 \right) n_w \quad (9)$$

where y_w is the distance from the wall and n_w is the normal to the wall. The coefficients C_{w1} and C_{w2} were set to -0.025 and 0.075 [6], respectively. This means the force only exists in a region of less than 5 bubble diameters from the wall.

The last term in eq. (4) represents the effect of the dispersion of the bubbles in a turbulent liquid flow. This force depends on the amount of turbulence in the continuous phase and the gradient of the volume fraction. Burns *et al.* [16] derived the turbulent dispersion force based on the Favre averaged drag model as

$$M_{lg}^{TD} = -M_{gl}^{TD} = C_{TD} C_{d,lg} \frac{v_l'}{\sigma_\alpha} \left(\frac{\nabla \alpha_g}{\alpha_g} - \frac{\nabla \alpha_l}{\alpha_l} \right) \quad (10)$$

where C_{TD} , v_l' , and σ_α are the turbulent dispersion coefficient, kinematic eddy viscosity, and volume fraction turbulent Prandtl number, respectively. The turbulent dispersion coefficient (C_{TD}) and turbulent Prandtl number (σ_α) were assumed to be 1.0 and 0.9, respectively. $C_{d,lg}$ is the resistance coefficient used to define the interphase drag model which can be expressed as

$$C_{d,lg} = \frac{3}{4} \frac{C_D}{d_b} \alpha_g \rho_l |U_g - U_l| \quad (11)$$

Heat transfer across a phase boundary with interphase mass transfer is handled by a two resistance model which considers separate heat transfer processes on either side of the phase interface. The two resistance model uses two heat transfer coefficients defined on each side of the phase interface. The fluid-specific heat transfer coefficient is expressed in terms of a non-dimensional Nusselt number:

$$Nu_k = \frac{h_k d_{lg}}{\lambda_k} \quad (12)$$

where λ_k is the thermal conductivity of phase k , and d_{lg} is a characteristic length scale, i.e., bubble diameter for a particle (bubble) in an incompressible fluid. The Nusselt number uses the well-known Ranz-Marshall correlation for the liquid side and is set to infinity for the vapour side. The infinite gas heat transfer coefficient (a zero resistance condition on the vapour side) is used to force the interfacial temperature to be the same as the vapour temperature. The Ranz-Marshall correlation is expressed as

$$Nu_l = 2 + 0.6 Re^{1/2} Pr^{1/3} \quad (13)$$

The mean bubble diameter is calculated locally as a linear function of liquid subcooling, as proposed by Anglart and Nylund [4], i.e.,

$$d_b = \frac{d_{b1} (T_{sub} - T_{sub,2}) + d_{b2} (T_{sub,1} - T_{sub})}{T_{sub,1} - T_{sub,2}} \quad (14)$$

Here, $d_{b1} = 0.1mm$, $T_{sub1} = 13.5K$, $d_{b2} = 2mm$, $T_{sub2} = -5K$.

The interphase mass transfer in a boiling flow includes the evaporation at the wall and bulk condensation or evaporation. The mass transfer from a liquid to vapour at the wall owing to evaporation is neglected in this CFD analysis. In the interior of the flow, the mass transfer rate between the two phases depends on the liquid temperature. When the liquid is subcooled, there is a bulk condensation from the vapour phase to the liquid. When the liquid is superheated, there is bulk evaporation from the liquid to the vapour. Both of these rates depend on the heat transfer rate and the latent heat (h_g).

$$\Gamma_{lg} = \max\left(\frac{h_l A_{lg} (T_{sat} - T_l)}{h_{lg}}, 0\right), \text{ for } T_l < T_{sat} \quad (15)$$

$$\Gamma_{gl} = \max\left(\frac{h_g A_{lg} (T_l - T_{sat})}{h_{lg}}, 0\right), \text{ for } T_l > T_{sat} \quad (16)$$

For a flow of spherical bubbles of diameter d_b in a liquid, the interfacial area density can be determined as

$$A_{lg} = \frac{6\alpha_g}{d_b} \quad (17)$$

The assumption for modeling the two-phase bubbly flow turbulence in the liquid phase is that the shear-induced turbulence and the bubble-induced turbulence can be superposed linearly. Hence, the turbulent viscosity of the liquid phase can be expressed as

$$\mu_l^t = \mu_l^{t(SI)} + \mu_l^{t(BI)} \quad (18)$$

The shear-induced turbulent viscosity is determined from the standard $k-\varepsilon$ model and the bubble-induced turbulent viscosity is expressed as (Sato *et al.*, [17])

$$\mu_l^{t(SI)} = \rho_l C_\mu \frac{k_l^2}{\varepsilon_l} \quad (19)$$

$$\mu_l^{t(BI)} = \rho_l C_{tb} \frac{d_b}{2} \alpha_g |U_g - U_l| \quad (20)$$

with coefficients of $C_\mu=0.09$ and $C_{tb}=1.2$.

2.2 Wall Boiling Model

The wall boiling model used in this study is the wall heat partition model (Kurul [2]) in which the total wall heat flux (Q_w) is split into three parts as illustrated in Fig. 1. These are the heat transfer rates owing to convection Q_f , quenching Q_q , and evaporation Q_e , i.e.,

$$Q_w = Q_f + Q_e + Q_q \quad (21)$$

The convective heat transfer rate is given in terms of the local Stanton number for a turbulent convection by:

$$Q_f = St \rho_l C_{pl} U_l (T_w - T_l) A_f \quad (22)$$

Here, T_w is the wall temperature and T_l and U_l are the liquid temperature and velocity in the cell next to the wall. A_f is the fraction of the wall area subjected to cooling by convection.

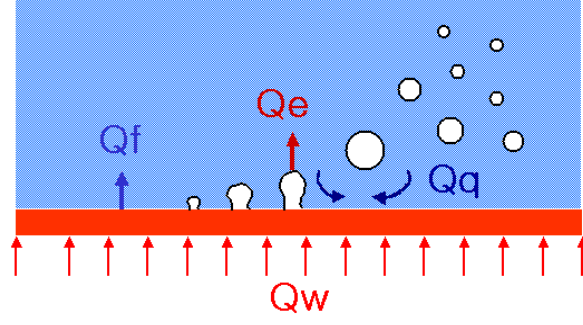


Figure 1: Schematic of wall boiling model.

A heat transfer from quenching is expected to occur when fresh liquid comes into contact with a heating surface after a bubble departs. This liquid is assumed to be heated by a transient conduction with a step change in the temperature at the surface. The corresponding heat transfer rate Q_q can be calculated by the relationship (Mikic and Rohsenow [18])

$$Q_q = \frac{2}{\sqrt{\pi}} f \sqrt{t_w \lambda_l \rho_l C_{pl}} (T_w - T_l) A_q \quad (23)$$

The heat flux owing to vapor generation at a heating surface can be expressed as

$$Q_e = nf \left(\frac{\pi}{6} d_{bw}^3 \right) \rho_g h_g. \quad (24)$$

The parameters used in Eqs. (23) and (24) are the nucleation site density (n), bubble detachment frequency (f), bubble departure diameter (d_{bw}), waiting time (t_w) and fraction of the wall area subjected to cooling by quenching (A_q). These parameters are given by the following correlations:

$$n = [185(T_w - T_{sat})]^{1.805} \quad (25)$$

$$f = \sqrt{\frac{4g(\rho_l - \rho_g)}{3d_{bw}\rho_l}}, \quad t_w = \frac{0.8}{f} \quad (26)$$

$$d_{bw} = \min \left[0.0006 \exp \left(-\frac{T_{sat} - T_l}{45} \right), 0.0014 \right] \quad (27)$$

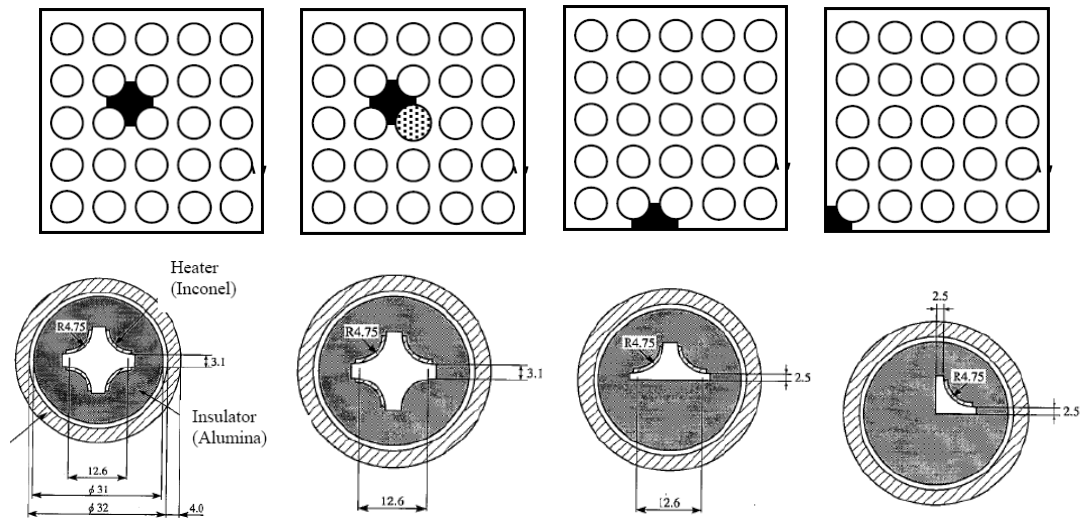
$$A_q = \min(\pi d_{bw}^2 n, 1), \quad A_f = 1 - A_q \quad (28)$$

3 CFD Model and Analysis

3.1 CFD Analysis of PSBT Benchmark Problem

This CFD study was performed to simulate single subchannel void distribution measurements for the OECD/NRC benchmark based on NUPEC PSBT [7]. The single subchannel test section is uniformly heated over 1555 mm by a direct heating method. The void measurement was made at 1400 mm from the bottom of the heated section. Figure 2 shows the test sections for the central typical, thimble, side, and corner subchannels. This CFD analysis analyzed the boiling flow in four different types of single subchannel. The twenty six (26) test cases in Table 1 were selected depending on the subchannel type and the test conditions. The inlet subcooling decreased from 97 °C to 14 °C for the typical subchannel

(S1) and 18 °C to 7 °C for the thimble subchannel (S2). The inlet subcoolings are 58 °C and 7 °C for the side and corner subchannels.



Typical subchannel (S1) Thimble subchannel (S2) Side subchannel (S3) Corner subchannel (S4)

Figure 2: Cross sectional view of the subchannel test assembly.

Table 1: PSBT test conditions.

Run No.	Subchannel type	Pressure (kg/cm ² a)	Mass flux (10 ⁶ kg/m ² hr)	Power (kW)	Inlet temperature (°C)	
1.1222	Typical(S1)	169	11	50.0	334.7	
1.1223		169	11	50.0	339.7	
1.2221		150	11	69.8	299.4	
1.2223		150	11	69.8	319.6	
1.2422		150	5	60.0	284.1	
1.2423		150	5	70.0	299.3	
1.4311		100	5	80.0	214.2	
1.4312		100	5	80.0	284.9	
1.5221		75	5	50.0	219.2	
1.5222		75	5	50.0	243.9	
1.6221		50	5	50.0	189.2	
1.6222		50	5	50.0	204.2	
2.1231		Thimble(S2)	169	11	37.5	335.0
2.1232			169	11	37.5	340.0
2.1233	169		11	37.5	345.0	
2.3232	125		11	45.1	309.8	
2.3233	125		11	45.1	319.9	
3.2231	Side(S3)	150	11	40.4	309.4	
3.2232		150	11	40.5	314.5	
3.2451		150	5	30.2	283.8	
3.2452		150	5	30.2	299.0	
3.2453		150	5	30.2	314.3	
4.2251	Corner(S4)	150	11	15.2	310.3	
4.2253		150	11	15.2	318.4	
4.2256		150	11	15.1	330.5	
4.2257		150	11	15.1	334.5	

Using the symmetry of the test section and flow, only the quadrant of the central (typical) subchannel and half of the side subchannel were modeled in this CFD analysis. Multi-blocks were employed to model the computational domain with a hexahedral mesh. The total number of meshes is 327000 cells for the quadrant subchannel. A uniform flow and constant temperature were assumed at the inlet boundary and a constant pressure was applied at the outlet boundary. A uniform heat flux and no-slip conditions were used at the heated wall.

Iterative calculations were performed to obtain a converged solution with a false time step and a high resolution differencing scheme (blending of first- and second-order upwind schemes). The numerical iteration was continued until both the root-mean-square (RMS) residuals of the governing equations and the variation of flow properties monitored at specified locations were insignificant. In addition, the velocity and volume fraction of liquid and vapor monitored at the outlet boundary were converged to their steady-state values. A CFD code, ANSYS CFX-12.1, was used to predict the void distribution inside the single subchannel.

3.2 CFD Analysis of BFBT Benchmark Problem

A full-scale BWR-simulated fuel assembly of an 8x8 rod bundle was installed in the NUPEC test facility. The heated length of the rod bundle is 3.708 m. Seven spacer grids are used to support the fuel rods in the bundle. The outer diameter of a fuel rod is 12.3 mm and the rod pitch is 16.2 mm. The subchannel-wise steady-state void distributions in the simulated BWR fuel assemblies were provided for the BFBT benchmark [8]. The benchmark exercise covered sixteen test series from five different test bundles, which included a different number of unheated rods and radial/axial power distributions. Four test cases (TS4101-53, 55, 58, 61) were selected for the microscopic void distribution benchmark.

Using the symmetry of the geometry and a radial power shape, half of the test assembly with a fully heated length (3.708m) was simulated in this CFD study. The spacers of the test bundle are not included in this CFD simulation because its effect on the void distribution is not judged to be large. A uniform flow and constant pressure are assumed at the inlet and outlet boundaries, respectively. A constant heat flux is applied on the fuel rods and adiabatic conditions on the water rod and shroud.

A hexahedral mesh is used and the total number of nodes is 4.72 million with 151 nodes in the streamwise direction. The lateral space between the nodes is 0.2 mm near the rod surface and 1.2 mm in the center of the subchannels. Figure 3 shows the cross-sectional view of the mesh used in this CFD analysis.

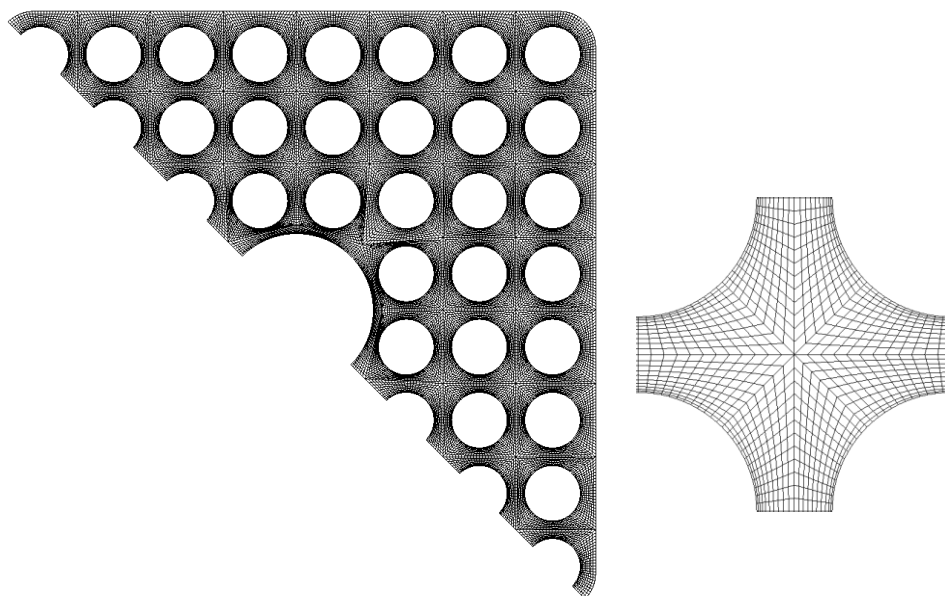


Figure 3: Cross-sectional mesh of the test bundle and the single subchannel for the CFD analysis.

An ANSYS CFX-10.0 code was used in this CFD study. Inhomogeneous multiphase flows were assumed to simulate the liquid and vapor phases, which are considered to be continuous and dispersed fluids, respectively. The vapor phase is assumed to be a spherical particle (bubble) with a mean diameter, d_b . Since the mean diameter of the vapor particle is unknown from the NUPEC measurements, it is assumed to be either constant (i.e., 2 mm) or to increase proportionally from the inlet to the exit of the test fuel bundle. The latter case assumed a vapor (bubble) diameter of 1 mm, 3 mm, 5 mm and 7 mm for a distance of 1 m, 2 m, 3 m, and 3.708 m from the inlet, respectively.

The two fluids interact via interphase transfer terms based on a particle model, i.e., interphase momentum transfer and heat transfer. The interfacial forces acting between two phases included in this study are the interphase drag, lift force, wall lubrication force, and turbulent dispersion force. This CFD analysis used the drag coefficient of the Ishii and Zuber correlation. The coefficients for the wall lubrication force, C_{w1} and C_{w2} , were set to -0.0064 and 0.05, respectively, which were recommended for the two-phase flow in a fuel-rod bundle [6]. The turbulent dispersion coefficient (C_{TD}) and turbulent Prandtl number (σ_α) were assumed to be 1.0 and 0.9, respectively. The value of lift force coefficient (C_L) is 0.01 for the case with a constant diameter of the vapor bubble. For the case with an increasing vapor bubble diameter (d_b), C_L changes from 0.03 at $d_b=1$ mm to -0.1 at $d_b=7$ mm.

The interphase heat transfer uses the two resistance model to consider separate heat transfer processes on either side of the phase interface. A constant Nusselt number (1000) is used for the liquid interphase heat transfer. A zero resistance condition for the interphase heat transfer is applied at the vapor side to force the interfacial temperature to be the same as the vapor-phase temperature, i.e., the saturation temperature.

Iterative calculations were performed to obtain a converged solution with a false time step and a high resolution differencing scheme. The numerical iteration was continued until both the root-mean-square (RMS) residuals of the governing equations and the variation of flow properties monitored at specified locations are insignificant. The RSM residuals of the governing equations were decreased to below 1×10^{-6} for the phasic momentum and volume fraction conservation, and 1×10^{-4} for the energy and turbulence conservation. In addition, the velocity and volume fraction of the liquid and vapor monitored at the outlet boundary were converged to their steady-state values.

4 Results and Discussion

4.1 CFD Results of PSBT Benchmark

The 26 test conditions in Table 1 were simulated in this CFD study, and their CFD results were compared with the measured values. Figure 4 compares the CFD predictions of void fraction in the subchannel with the CT images for the three cases of Run No. 1.1222, 1.2223, and 1.2423. The predicted void contours show less vapour in the core region and high vapour in the gap region and the near-wall region, which agrees well with the CT measurements. It should be noted in the CT image that the vapour seems to move significantly into the gap region for the high void condition (Run No. 1.2423). However, the CFD prediction shows a high void fraction near the heated rod wall.

Table 2 lists the subchannel averaged fluid density and void fraction at the measurement plane (1.4 m from the bottom of the test section). The CFD predictions agree well with the measured values for the low subcooling conditions (e.g., < 30 °C) such as Run No. 1.1223, 1.2223, 2.3232, 2.3233, 4.2256 and 4.2257). However, the CFD calculations tend to overpredict the void fraction and underpredict the fluid density as the inlet subcooling increases. For the high subcooling condition (Run No. 1.6221), the CFD predictions show a void fraction of as high as 19% and fluid density of as low as 10%. Figure 5 compares the CFD predictions of the void fraction and fluid density with the measured values. It can be seen that the CFD predictions agree with the experimental data within 10% for the void fraction and the fluid density, respectively.

The effects of non-drag forces and turbulence model are shown in Fig. 6 for the test run 1.1222. The non-drag forces show a strong influence for the radial void distribution near the rod wall. The lift force and turbulent dispersion force (TD) appear to push the vapour bubble into the wall boundary, while the wall lubrication force (LW) directs the bubble to the core region. The void fraction without

the LW shows a peak at the wall. The SSG Reynolds stress model predicted a higher void fraction in the core region as well as in the near-wall region. This is because the secondary flow predicted by the Reynolds stress model moves the bubble in the lateral direction.

Table 2: Subchannel averaged void fraction and fluid density.

Run No.	Fluid density(kg/m ³)		Void fraction	
	PSBT	CFD	PSBT	CFD
1.1222	517	500	0.142	0.196
1.1223	434	465	0.332	0.257
1.2221	621	609	0.048	0.066
1.2223	456	441	0.311	0.338
1.2422	522	465	0.182	0.298
1.2423	357	389	0.508	0.430
1.4311	563	477	0.215	0.343
1.4312	331	321	0.566	0.572
1.5221	718	597	0.047	0.211
1.5222	448	393	0.411	0.488
1.6221	737	587	0.075	0.261
1.6222	549	447	0.306	0.438
2.1231	550	542	0.096	0.125
2.1232	501	505	0.181	0.183
2.1233	430	466	0.333	0.246
2.3232	539	521	0.202	0.240
2.3233	608	437	0.409	0.370
3.2231	553	548	0.041	0.164
3.2232	637	514	0.132	0.219
3.2451	551	560	0.007	0.147
3.2452	372	472	0.111	0.288
3.2453	608	390	0.469	0.433
4.2251	636	635	0.003	0.046
4.2253	602	587	0.028	0.105
4.2256	498	506	0.226	0.218
4.2257	438	474	0.307	0.269

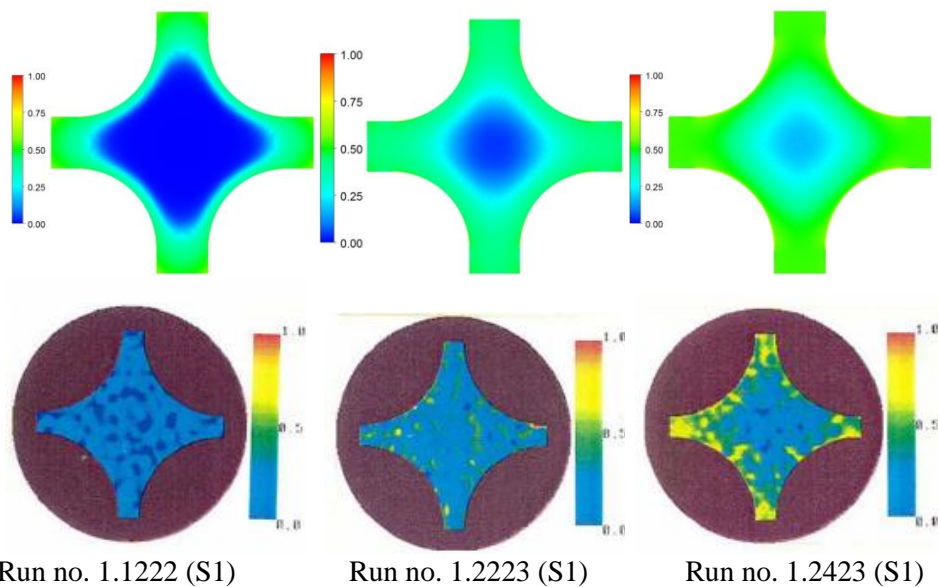


Figure 4: Void fraction contour in the subchannel: (upper) CFD, (low) CT image.

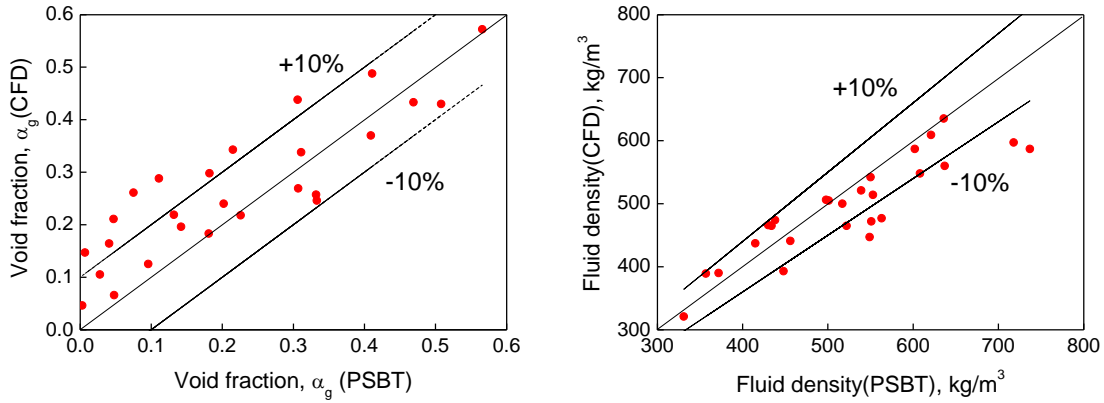


Figure 5: Comparisons of void fraction and fluid density in the subchannel.

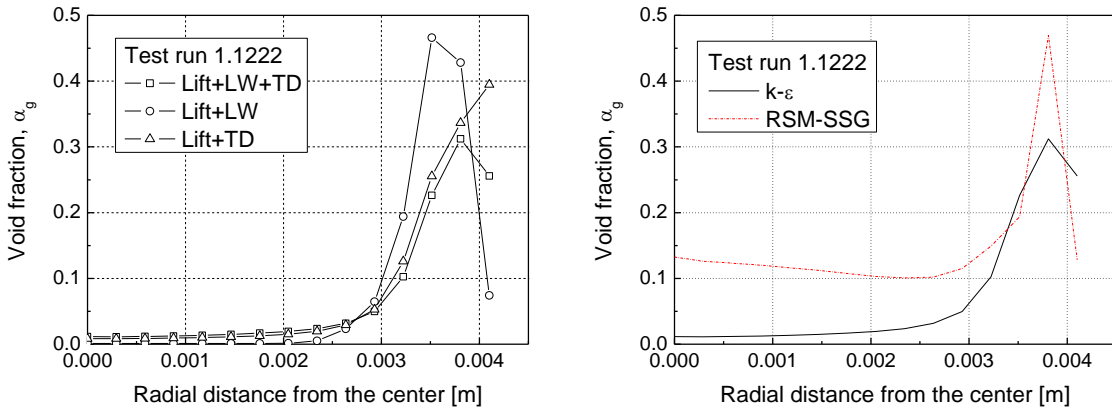


Figure 6: Effects of Non-drag forces and turbulence model.

4.2 CFD Results of BFBT Benchmark

Four test cases (TS4101-53, 55, 58, 61) were simulated using ANSYS CFX-10 in this CFD study to predict the steady-state void distribution in test assembly 4. The CFX simulations were performed using two sets of mean bubble diameter and lift force coefficient since they are known to be important parameters for the void distribution. The first CFX simulation (CFX1) used the lift coefficient of 0.01 with the constant mean bubble-diameter of 2 mm. The second case (CFX2) is the CFX simulation with a variable lift coefficient depending on the bubble diameter, which increases downstream of the test section. The CFX predictions of the void distribution are compared with the experimental data at fine-mesh grade and subchannel grade.

The void distributions at the exit of the test bundle are compared in Fig. 7 for the test case TS4101-55. The measured one shows the raw image data obtained from the X-ray CT scanner which has a spatial resolution as small as 0.3 mm x 0.3 mm. The CFX simulation shows a reasonable radial void distribution trend predicting less vapor in the central region of the bundle and more vapor in the periphery. This trend is consistent with the radial power distribution, which is diagonally symmetric. The CFX1 prediction shows a higher concentration of vapor near the rod surfaces instead of in the center of the subchannels. Similarly to the measured data, the CFX2 case predicted a higher void fraction in the center of the subchannels and a lower void near the rod surface. This is because the CFX2 simulation used a negative value of the lift force coefficient with a large bubble diameter near the exit of the test assembly.

Table 3 summarizes the cross-sectional averaged void fraction at the exit of the heated section. The CFX1 predictions agree well with the measurements for the conditions of a low exit quality, but tend to be lower than the measured values for the high quality cases. The CFX1 predictions agree with

the measured values within 1% for the low exit quality conditions (TS4101-53, -55) and 10% for the high exit quality conditions (TS4101-58, -61). The CFX2 case with a variable lift coefficient and vapor size tends to predict the bundle-averaged void fraction lower than the CFX1 case. The under-prediction of the CFX2 case appears to increase as the exit quality decreases.

Table 3: Cross-sectional averaged exit void fraction (%) for test assembly 4.

Test Case	CFX1	CFX2	BFBT Data
TS4101-53	24.7	-	25.0
TS4101-55	43.4	37.2	43.8
TS4101-58	59.2	56.5	64.5
TS4101-61	70.9	68.1	80.7

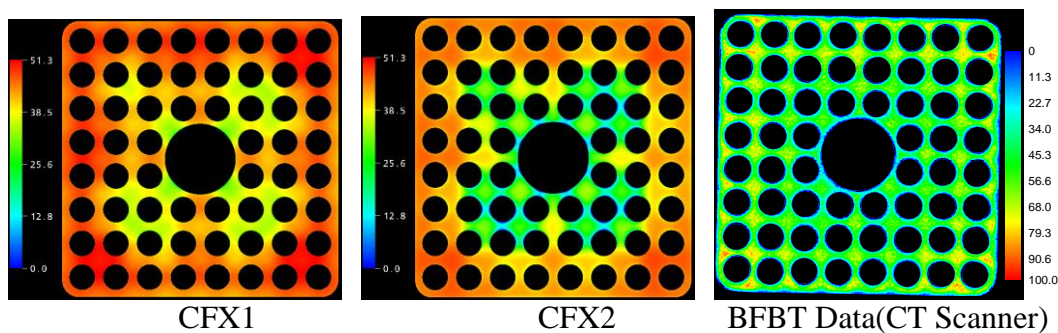


Figure 7: Void distributions at the exit of test assembly 4 for the TS4101-55 case.

Figure 8 compares the CFX1 predictions of the subchannel void distribution with the measured values. The predicted void fraction tends to be lower than the measured value as the exit quality (or bundle-average void fraction) increases. The under-prediction of the void fraction is estimated to be 5% and 10% for TS4101-58 and TS4101-61, respectively. The CFX1 prediction agrees well with the experimental data for the low exit quality condition (TS4101-53) even if a large under-prediction is noted in few subchannels (No. 21, 24, 25, 47, 48, 50, 51, 56, 57, 59, 60) surrounding the fuel rod with low power. The CFX1 also predicts the variation of the subchannel void fraction to significantly decrease for the high exit quality conditions, i.e., TS4101-58 and TS4101-61. The CFX2 predictions for TS4101-55 show a larger variation of the subchannel void fraction than the CFX1 case.

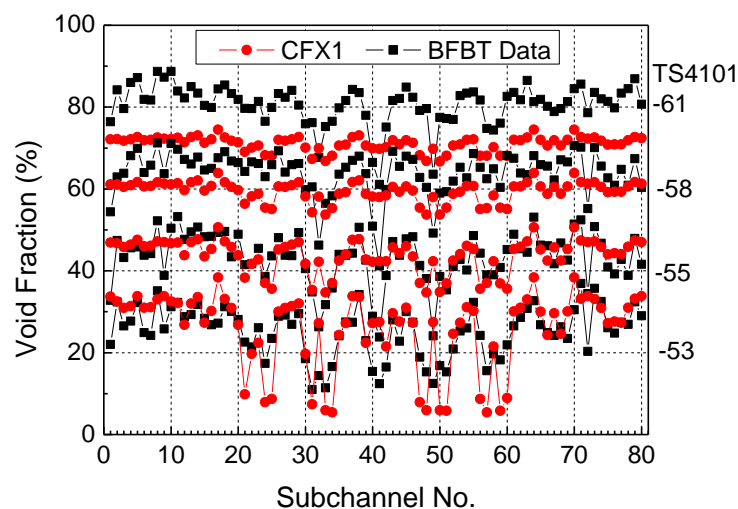


Figure 8: Comparisons of the subchannel void distributions for the BFBT benchmark.

Figure 9 compares the lateral local void distribution along the centerline through the subchannels in the second and third rows of the test assembly, i.e., an 8x8 rod array. The measurement accuracy of 8% for local void fraction is illustrated in Fig. 9. The CFX simulations predict a much lower void than the measured value particularly in the center of the subchannels. The variation of the void fraction between the subchannel center and the rod gap is about 5%-10% for the CFX simulations and 20%-30% for the measured value. The CFX2 case predicted a somewhat larger variation of the void distribution in the third rows of the subchannels than the CFX1 case. It is also noted that the CFX2 case was able to predict the void peaking measured at the center of the subchannels. The large discrepancy between the CFX predictions and the measured values appears to be caused by the uncertainties in the size and shape of the vapor phase and the use of the interfacial closure models assuming a spherical vapor for the vapor phase.

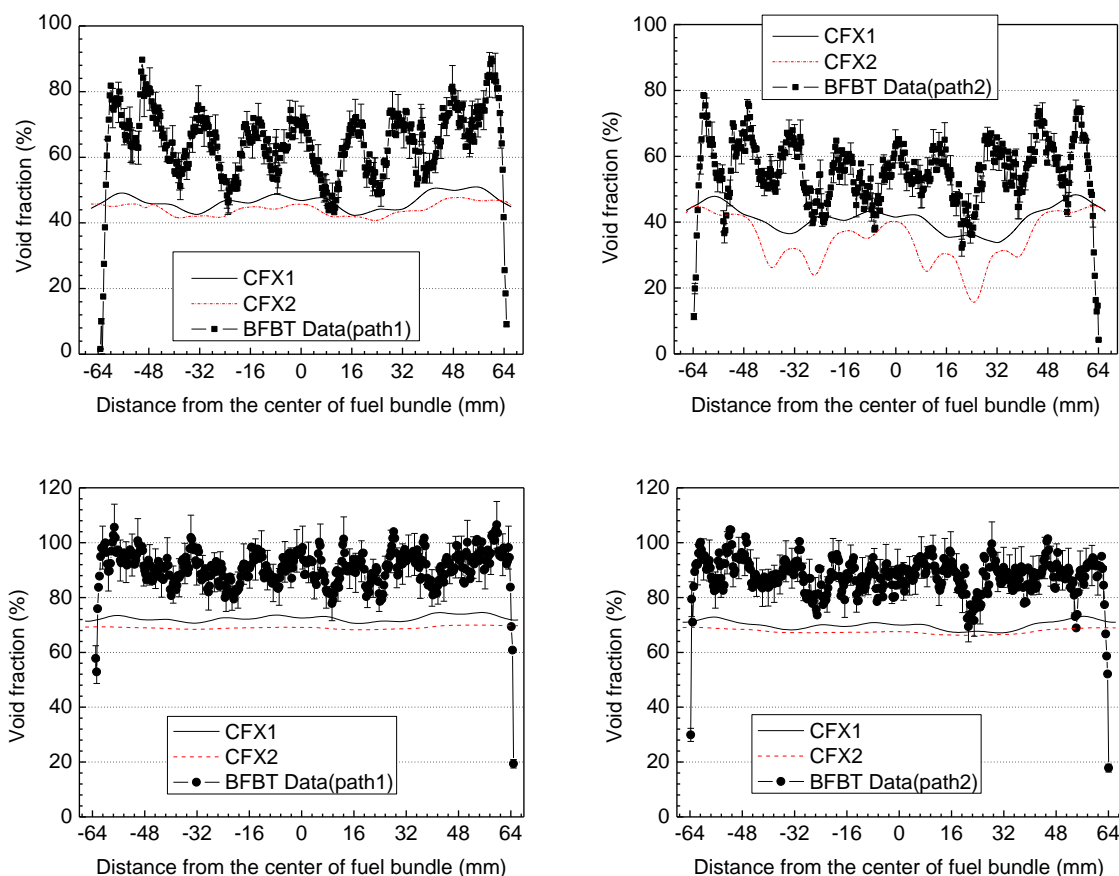


Figure 9: Lateral void distribution along the centerline through the subchannels located in the second (path1) and third rows (path2) of test assembly 4 for the TS4101-55 (top) and TS4101-61 (bottom) cases.

5 Conclusion and Future Work

A CFD analysis was performed to simulate the subcooled boiling flows in the subchannels of PWR and BWR fuel bundles. The CFD results can be summarized as follows:

- (1) The CFD predictions for the PWR subchannel benchmark agree with the experimental data within 10% for the void fraction and the fluid density at the low inlet subcooling (<30 °C), and over estimate the void fraction as the inlet subcooling increases.
- (2) The CFD simulation of the BWR benchmark problem predicted the cross-sectional averaged void fraction, which agrees with the measured values within 1% and 10% for the low and high exit

quality conditions, respectively. The subchannel void distribution obtained from the CFD prediction appeared to be lower than the measured value and shows a small variation as the bundle-exit quality increases.

- (3) The non-drag forces showed a strong influence on the radial distribution of the void fraction near the rod wall. The CFD calculation with a negative lift force coefficient was able to predict the void peaking measured at the center of the subchannels.
- (4) The mechanistic models for the bubble size, interfacial closure models, and multiphase turbulence should be developed in the future to enhance the reliability and consistency of the multiphase CFD method in nuclear thermal-hydraulics.

Acknowledgement

The authors are very grateful to the OECD NUPEC BFBT and PSBT Benchmark Programs, through which the valuable experiment data for the code assessment was obtained. The authors thank Dr. Utsuno at NUPEC, Prof. Ivanov at Penn. State University, and Mr. Sartory at OECD for their efforts for the benchmark program. This work has been performed as a part of the Nuclear Research and Development Program supported by the Ministry of Education, Science and Technology of the Republic of Korea.

References

- [1] G. Yadigaroglu, M. Andreani, J. Dreier and P. Coddington. Trends and needs in experimentation and numerical simulation of LWR safety. *Nuclear Engineering and Design*, 221:205-223, 2003.
- [2] N. Kurul. *Multidimensional effects in two-phase flow including phase change*, Ph. D. Thesis, Rensselaer Polytechnic Institute, 1990.
- [3] H. Anglart. Modeling of vapor generation rate at wall in subcooled boiling two-phase flow. First CFDS International User Conference, Oxford, UK, pp.183-207, 1993.
- [4] H. Anglart and O. Nylund. CFDS application to prediction of void distribution in two-phase bubbly flows in rod bundles. *Nuclear Science and Engineering*, 163:81-99, 1996.
- [5] G. H. Yeoh and J. Y. Tu. Numerical simulation of subcooled boiling flow in an annular channel with the influence of bubble coalescence and break-up. *The 10th International Topical Meeting on Nuclear Reactor Thermal Hydraulics(NURETH-10)*, Seoul, Korea, October 5-9, 2003.
- [6] E. Krepper, B. Koncar and Y. Egorov. CFD modeling of subcooled boiling – concept, validation and application to fuel assembly design. *Nuclear Engineering and Design*, 237:716-731, 2007.
- [7] A. Rubin, et al. *OECD/NRC benchmark based on NUPEC PWR subchannel and bundle tests (PSBT) – Vol. I*. NEA/NSC/Doc(2010), 2010.
- [8] B. Neykov, et al. *NUPEC BWR full-size fine-mesh bundle test benchmark (BFBT) – Vol. I*. NEA/NSC/Doc(2005), 2005.
- [9] ANSYS Inc., *ANSYS CFX-Solver*, Release 10.0(2005) & 12.1(2009).
- [10] M. Ishii and K. Mishima K. Two-fluid modeling and hydrodynamic constitutive relations. *Nuclear Engineering and Design*, 82:107-126, 1984.
- [11] M. Ishii and M. Zuber. Drag coefficient and relative velocity in bubbly, droplet or particulate flows. *AIChE J.*, 25:843-855, 1979.
- [12] I. Zun. The transverse migration of bubbles influenced by walls in vertical bubbly flow. *Int. J. Multiphase Flow*. Vol. 6(6):583-588, 1980.
- [13] A. Tomiyama, H. T. Tamai, I. Zun and S. Hosokawa. Transverse migration of single bubbles in simple shear flows. *Chemical Engineering and Science*, 57:1849-1858, 2002.
- [14] T. Hibiki and M. Ishii. Lift force in bubbly flow systems. *Chemical Engineering and Science*, 62:6457-6474, 2007.
- [15] S. P. Antal, R. T. Lahey Jr. and J. E. Flaherty. Analysis of phase distribution in fully developed

- laminar bubbly two-phase flow. *Int. J. Multiphase Flow*, 17(5):635-652, 1991.
- [16] A. D. Burns, T. Frank, I. Hamill and J. Shi, The Favre averaged drag model for turbulent dispersion in Eulerian multi-phase flows, *ICMF'2004, 5th International Conference on Multiphase Flow*, Yokohama, Japan, 2004.
- [17] Y. Sato, M. Sadatomi and K. Sekoguchi. Momentum and heat transfer in two-phase bubbly flow – I. *Int. J. Multiphase Flow*, 7:167-177, 1981.
- [18] B. B. Mikic and W. M. Rohsenow. A new correlation of pool-boiling data including the fact of heating surface characteristics. *ASME J. Heat Transfer*, 91:245-250. 1969.